Performance Optimization Criteria for Pulsed Inductive Plasma Acceleration

Kurt A. Polzin and Edgar Y. Choueiri

***Abstract*—A model of pulsed inductive plasma thrusters consisting of a set of coupled circuit equations and a one-dimensional momentum equation has been nondimensionalized leading to the identification of several scaling parameters. Contour plots representing thruster performance (exhaust velocity and efficiency) were generated numerically as a function of the scaling parameters. The analysis revealed the benefits of underdamped current waveforms and led to an efficiency maximization criterion that requires the circuit's natural period to be matched to the acceleration timescale. It is also shown that the performance increases as a greater fraction of the propellant is loaded nearer to the inductive acceleration coil.**

***Index Terms*—Acceleration modeling, nondimensional scaling parameters, pulsed inductive acceleration, pulsed plasma acceleration.**

I. Introduction

PULSED inductive plasma accelerators are spacecraft propulsion devices in which energy is stored in a capacitor and then discharged through an inductive coil. The device is electrodeless, inducing a current in a plasma located near the face of the coil. The propellant is accelerated and expelled at a high exhaust velocity ($\mathcal{O}$ (10 km/s)) by the Lorentz force arising from the interaction of the plasma current and the induced magnetic field [see Fig. 1(a) for a thruster schematic]. Presently, there are two concepts which operate on this principle. One is the pulsed inductive thruster (PIT) [1], in which both propellant ionization and acceleration are performed by the pulse of current flowing through the inductive coil. In contrast, the Faraday accelerator with radio-frequency assisted discharge (FARAD) [2] uses a separate inductive discharge (radio frequency/helicon discharge) to pre-ionize the propellant before it is accelerated by the current pulse in the coil.

Inductive plasma accelerators are attractive as propulsive devices for many reasons. The lifetime and contamination issues associated with electrode erosion in conventional pulsed plasma thrusters (PPTs) do not exist in devices where the discharge is inductively driven. In addition, a wider variety of propellants (e.g., CO_2, H_2O) becomes available for use when compatibility with metallic electrodes is no longer an issue. Moreover, pulsed inductive accelerators (indeed, pulsed accelerators in general) can maintain the same performance level over a wide range of input power levels by adjusting the pulse rate.

Manuscript received June 26, 2005; revised October 23, 2005.

K. A. Polzin is with the NASA-Marshall Space Flight Center, Huntsville, AL 35812 USA (e-mail: kurt.a.polzin@nasa.gov).

E. Y. Choueiri is with the Electric Propulsion and Plasma Dynamics Laboratory, Mechanical and Aerospace Engineering Department, Princeton University, Princeton, NJ 08544 USA (e-mail: choueiri@princeton.edu)

Digital Object Identifier 10.1109/TPS.2006.875732

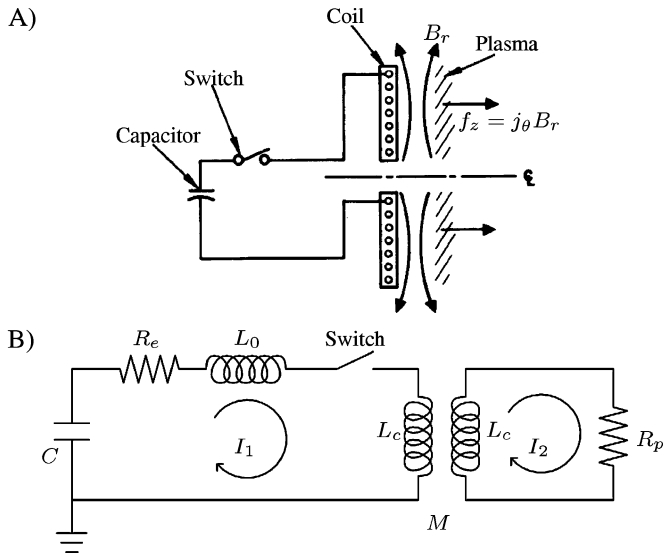

Fig. 1. (a) Conceptual schematic (from [5]) and (b) general lumped element circuit model (after [5]) of a pulsed inductive accelerator.

In PPT research, there has been substantial effort devoted to the development of simple one-dimensional (1-D) acceleration models (cf. [3]). These models typically consist of a circuit equation coupled to a 1-D momentum equation in which propellant is accumulated, or "snowplowed," by a current sheet that is accelerated by the Lorentz body force. These models have led to the identification of nondimensional scaling parameters that have proved insightful in PPT research [3], [4].

There also exists a 1-D pulsed inductive acceleration model similar to the type used in PPT analysis [1], [5]. This model differs from its PPT counterpart in that it must account for a second, inductively coupled circuit in the circuit equations. Unfortunately, since there has not been work analogous to the PPT research in deriving and interpreting physically meaningful parameters, designs of pulsed inductive accelerators are currently being performed using a set of empirical rules found to work over the years. The purpose of the present paper is to identify nondimensional scaling parameters that control accelerator performance (exhaust velocity and thrust efficiency). When possible, we shall attempt to use the corresponding PPT nondimensional parameters to aid in the physical interpretation of the inductive acceleration terms.

The outline for the rest of this paper is as follows. In Section II, the dimensional equations governing the operation of a pulsed inductive accelerator are first presented and then nondimensionalized to yield the relevant scaling parameters. In the following section, the physical meanings of the various

scaling parameters are distilled using both an understanding gained from past PPT research and some limiting-case solutions to the nondimensional equation set. In Section IV, performance of a pulsed inductive accelerator is computed by solving the full nondimensional equation set as a function of the nondimensional parameters. Contours of constant accelerator performance are plotted, and specific features and trends in the data as a function of the various scaling parameters are interpreted based upon the physical insight gained in the previous section. The computed performance contours lead to additional physical insights into the acceleration process which are discussed in Section V.

II. Governing Equations

A. Dimensional Equation Set

A circuit-based model of a pulsed inductive accelerator has been previously developed by Lovberg and Dailey [5]. In the present paper, we shall briefly review the equation set and refer the reader to the earlier work for more detailed derivations of the equations.

1) Circuit Equations: A lumped-element circuit model of a pulsed inductive accelerator is presented in Fig. 1(b). The external circuit (left side of the figure) possesses capacitance C, external inductance L_0, resistance R_e, and acceleration coil inductance L_C. The plasma also has an inductance equal to L_C and a resistance R_p. The two circuits are inductively coupled through the acceleration coil, which acts as a transformer with mutual inductance M. The value of M is a function of the current sheet position z. The time-varying behavior of this circuit is governed by the following coupled set of first-order ordinary differential equations:

$$\begin{aligned}\frac{dI_1}{dt} &= \frac{VL_C + (MI_1 + I_2L_C)\frac{dM}{dt} - I_2MR_p - I_1R_eL_C}{L_C(L_0 + L_C) - M^2}\\ \frac{dI_2}{dt} &= \frac{M\frac{dI_1}{dt} + I_1\frac{dM}{dt} - I_2R_p}{L_C}\\ \frac{dV}{dt} &= -\frac{I_1}{C}\end{aligned} \tag{1}$$

where V is the voltage on the capacitor. Based on experimental measurements, it has been found [5] that the mutual inductance in the system can be modeled using the exponential function

$$M = L_C \exp\left(-\frac{z}{2z_0}\right) \tag{2}$$

where z_0 is defined as the decoupling length. The preceding equation can be differentiated to yield

$$\frac{dM}{dt} = -\frac{L_C}{2z_0}\exp\left(-\frac{z}{2z_0}\right)\frac{dz}{dt} \tag{3}$$

which governs the time-varying behavior of the mutual inductance and completes the set of circuit equations.

2) Momentum Equation: In the idealized "snowplow" model, as the current sheet moves forward, it entrains and accelerates any gas that it encounters. The propellant mass in the current sheet as a function of time can be written as

$$m(t) = m_0 + \int_{t=0}^{t} \rho_A v_z dt \tag{4}$$

where $\rho_A = \rho_A(z(t))$ is the linear mass density distribution and v_z is the sheet velocity. The term m_0 represents the initial mass of propellant in the sheet while the integral term represents the mass accumulated by the sheet as it moves away from the acceleration coil. (Note that while the ideal snowplow model is often employed in pulsed plasma modeling, the current sheet in a real accelerator entrains only a fraction of the total available propellant, depending largely upon the plasma properties in the current sheet.)

The momentum equation for this system can be written as

$$\frac{L_C I_1^2}{2z_0}\exp(-z/z_0) = \rho_A v_z^2 + m(t)\frac{dv_z}{dt}. \tag{5}$$

The left-hand side represents the self-field electromagnetic force while the first term on the right-hand side represents the momentum investment associated with entraining the propellant and the second term involves further acceleration of the already entrained propellant.

3) Plasma Model: We shall not employ a plasma model in this study. However, in general, a model of the plasma is required to close the set of equations. Such detailed modeling is the subject of ongoing work in inductive plasma acceleration [7]–[9], but it is beyond the scope of the present study, which instead aims at gaining a basic understanding of the scaling in a pulsed inductive accelerator. In previous studies [1] using the simplified 1-D model described in this section, the energy equation was eliminated by explicitly assuming a value for the electron temperature that yielded a quantitative match between experimental performance data and numerical simulations. This assumption allowed for an approximate computation of the plasma resistance R_p.

B. Additional Shortcomings of the Acceleration Model

We have already discussed some of the differences between the acceleration model and a real pulsed inductive thruster. The most important additional assumptions embedded in the model are that current sheet formation is immediate (at $t = 0$) and complete (does not allow the induced magnetic field to diffuse through it for all time). In experiments, while the current sheet does form quite early during the first half-cycle of the discharge, it does not form "immediately" nor is it perfectly impermeable to the induced magnetic field [10]. The lack of an ionization model results in an inability to capture transient plasma physics phenomena. This is especially important during the breakdown stage, where the assumption of constant-value lumped circuit elements is violated. Evidence of this idealization is presented in Fig. 2 where we compare experimental data from [6] with a numerical solution to the governing equations. Though the waveforms show reasonably good agreement, we do note some departure during the initial rise which persists throughout the first half-cycle. An even greater departure starting at around $t =$

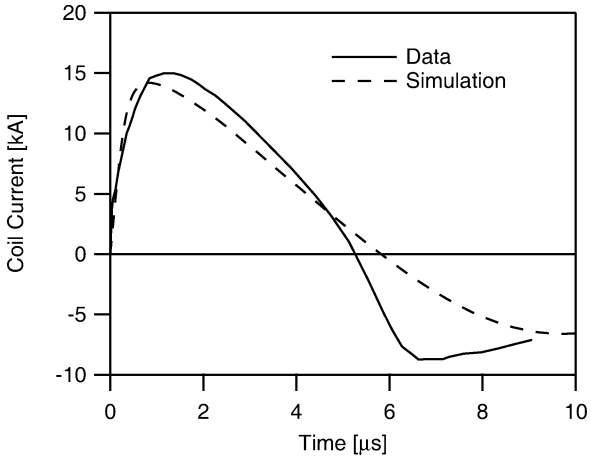

Fig. 2. Comparison of experimentally acquired (solid line, from [6]) and numerically generated (dashed line) current traces in the PIT.

5 μs is likely due to a second "crowbar" discharge forming at the coil face.

In the present paper, we sidestep many of the model's shortcomings, only using the model as a tool to search for relevant nondimensional scaling parameters and performance trends. We do note, however, that exhaust velocities and thruster efficiencies predicted by 1-D, circuit-based acceleration models, even with all their shortcomings, show good qualitative and quantitative agreement with experimental performance data for both inductive thrusters [1] and PPTs [4].

C. Nondimensional Equations

Following Ziemer and Choueiri's modeling of a PPT [4], we nondimensionalize the inductive accelerator's set of governing equations in an attempt to identify relevant scaling parameters and find their optimum values. However, differences between the models for these two accelerators arise due to the following.

1) In the inductive thruster acceleration, there are two dependent current loops while there is only the one loop in PPTs.
2) The mutual inductance term also does not appear in PPT modeling; however, it is essential to the coupling between the two current loops in an inductive accelerator.

We also recall that the inductive acceleration model we are employing lacks a model of the plasma. Our strategy of finding nondimensional scaling parameters and searching for physical insight instead of attempting to exactly model an accelerator allows us to bypass this issue. As an exercise, we could simply vary any dimensionless parameter which contains R_p to determine the sensitivity of the acceleration process. Using the prescription given in [1], we estimate a plasma resistance between $\mathcal{O}(10\text{–}100\ \mathrm{m}\Omega)$ in the PIT MkV.

The following dimensionless terms can be readily selected as a starting point based upon prior knowledge of PPT scaling laws:

$$\begin{aligned} I_1^* &= \frac{1}{V_0}\sqrt{\frac{L_0}{C}}I_1 \\ I_2^* &= \frac{1}{V_0}\sqrt{\frac{L_0}{C}}I_2 \\ t^* &= \frac{t}{\sqrt{L_0 C}}. \end{aligned} \tag{6}$$

In the course of nondimensionalizing the governing equations the following additional nondimensional variables naturally appear in the equation set:

$$\begin{aligned} z^* &= \frac{z}{z_0} \\ V^* &= \frac{V}{V_0} \\ M^* &= \frac{M}{L_C} \\ v_z^* &= \frac{\sqrt{L_0 C}}{z_0}v_z. \end{aligned} \tag{7}$$

In the framework of (4), the propellant can either be loaded as a slug mass ($\rho_A = 0$ for all z) or as some function of position ($\rho_A = \rho_0 f(z)$). If the propellant is loaded as a slug mass and we nondimensionalize by the propellant mass per shot, m_{bit}, the nondimensional mass accumulation statement can be written as

$$m^* = \frac{m}{m_{\mathrm{bit}}} = 1 \quad \text{for all time.} \tag{8}$$

For a propellant loading which is a function of z, we obtain the statement

$$m^* = m_0^* + \int_0^{t^*} \rho^* f(z^*) v_z^* dt^* \tag{9}$$

where $m_0^* = m_0/m_{\mathrm{bit}}$ and $\rho^* = \rho_0 z_0/m_{\mathrm{bit}}$.

Writing (1), (3), (5), and (9) in terms of the dimensionless variables and in differential form, we obtain

$$\begin{aligned} \frac{dI_1^*}{dt^*} &= \left[L^*V^* + (M^*I_1^* + I_2^*)(dM^*/dt^*) - I_2^*M^*L^*\psi_2 \right. \\ &\quad \left. - I_1^*L^*\psi_1\right] / \left[(L^*+1) - (M^*)^2\right] && \text{(10a)} \\ \frac{dI_2^*}{dt^*} &= M^*\frac{dI_1^*}{dt^*} + I_1^*\frac{dM^*}{dt^*} - I_2^*L^*\psi_2 && \text{(10b)} \\ \frac{dV^*}{dt^*} &= -I_1^* && \text{(10c)} \\ \frac{dM^*}{dt^*} &= -\frac{1}{2}\exp\left(-\frac{z^*}{2}\right)v_z^* && \text{(10d)} \\ \frac{dz^*}{dt^*} &= v_z^* && \text{(10e)} \\ \frac{dv_z^*}{dt^*} &= \left[\alpha\,(I_1^*)^2\exp(-z^*) - \rho^* f(z^*)\,(v_z^*)^2\right]/m^* && \text{(10f)} \\ \frac{dm^*}{dt^*} &= \rho^* f(z^*) v_z^*. && \text{(10g)} \end{aligned}$$

The relevant scaling parameters which emerge from the system of equations are defined as

$$\begin{aligned} L^* &= \frac{L_0}{L_C} \\ \psi_1 &= R_e\sqrt{\frac{C}{L_0}} \\ \psi_2 &= R_p\sqrt{\frac{C}{L_0}} \\ \alpha &= \frac{C^2V_0^2L_C}{2m_{\mathrm{bit}}z_0^2}. \end{aligned} \tag{11}$$

The initial conditions for the set of nondimensional differential equations are

$$\begin{aligned} I_1^*(0) &= 0, \qquad I_2^*(0) = 0, \\ V^*(0) &= 1, \qquad M^*(0) = 1, \\ z^*(0) &= 0, \qquad v_z^*(0) = 0, \\ m^*(0) &= \frac{m_0}{m_{\text{bit}}}. \end{aligned}$$

Note that when the propellant is loaded like a slug, the right-hand side of (10g) and the second term on the right-hand side of (10f) disappear ($\rho^* = 0$).

III. Interpretation of the Scaling Parameters

A. Inductance Ratio: L^*

It is well known that the efficiency of a pulsed electromagnetic accelerator cannot exceed the fractional change of inductance, $\Delta L/L_0$ (see [11]). This ratio is a measure of the fraction of energy that can be deposited into electromagnetic acceleration of the gas. Recognizing from (2) that L_C is equal to the total inductance change available to the accelerator (i.e., $L_C = \Delta L$) allows us to write $(L^*)^{-1} = \Delta L/L_0$. Consequently, we expect the value of L^* to be less than unity in an efficient pulsed inductive accelerator.

B. Critical Resistance Ratios: ψ_1 and ψ_2

Like their counterpart found in the gas-fed PPT literature [4], the ratios ψ_1 and ψ_2 appear in the circuit equations and control the nature of the current waveforms.

To determine the physical meanings of ψ_1 and ψ_2, we attempt to find limiting solutions to (10a)–(10c). Decoupling the current sheet dynamics (i.e., the acceleration and sheet motion) from the problem allows us to apply the following condition:

$$M^* = 1$$

which dramatically simplifies the circuit equations. Under this assumption, the circuit equations can be rewritten as

$$\begin{aligned} \frac{d^2 I_1^*}{dt^{*2}} + (\psi_1 + \psi_2)\frac{dI_1^*}{dt^*} + I_1^* &= \psi_2^2 L^* I_2^* \\ \frac{dI_1^*}{dt^*} - \frac{dI_2^*}{dt^*} &= \psi_2 L^* I_2^*. \end{aligned} \tag{12}$$

If the right-hand side of first equation is small (≈ 0), then the solution for I_1 is

$$I_1^* = A_0 \exp(-\Psi t^*)\, \sin\left((1-\Psi^2)^{1/2}\, t^*\right)$$

where we have introduced the new dimensionless parameter $\Psi \equiv (\psi_1 + \psi_2)/2$. The solution is underdamped (ringing) for $\Psi < 1$, critically damped for $\Psi = 1$, and overdamped for $\Psi > 1$. If the right–hand side in the second of (12) is also small, then the induced current in the plasma mirrors the current in the coil

$$I_2^* = I_1^*.$$

The fact that the current waveform depends on the sum of ψ_1 and ψ_2 implies that within a portion of the (ψ_1, ψ_2) parameter space, contours of constant performance should generally follow the contours given by the equation

$$(\psi_1 + \psi_2)/2 = \text{constant}.$$

To neglect the nonlinearities present in the circuit equations and arrive at the limiting solutions given above, the values of L^* and ψ_2 must be such that

$$\begin{aligned} \psi_2^2 L^* &\ll 1 \\ \psi_2 L^* &\ll 1. \end{aligned}$$

Therefore, we expect a feature or transition in a contour plot of accelerator performance as either $\psi_2^2 L^*$ or $\psi_2 L^*$ approaches unity.

C. Dynamic Impedance Parameter: α

The parameter α is similar to the one found in the PPT literature [3], [4]. Following Jahn [3], we can write α as the product of several important ratios

$$\alpha = \frac{C^2 V_0^2 L_C}{2 m_{\text{bit}} z_0^2} = \frac{1}{8\pi^2}\frac{C V_0^2/2}{m_{\text{bit}} v_z^2/2} L^* \left(\frac{2\pi\sqrt{L_0 C}}{L_0/\dot{L}}\right)^2$$

where $\dot{L}$ is the dynamic impedance which is defined as $v_z L'$ and L' is defined as an effective inductance per unit length equal to L_C/z_0. The ratios written on the right-hand side of the first line are identified as follows.

- The ratio of the initial stored energy to the plasma kinetic energy, which is also the inverse of thrust efficiency. This term will always be greater than one.
- The inductance ratio L^* which will typically be less than one in an efficient electromagnetic accelerator.
- The ratio of the resonant period of the unloaded circuit, $2\pi\sqrt{L_0 C}$, to the time it takes for the circuit to increase its inductance by L_0, which is equal to $L_0/\dot{L}$.

The term $L_0/\dot{L}$ identified in the final bullet point above is essentially the time scale on which the current sheet remains in the acceleration region before decoupling from the coil (i.e., residence time). The other term, $2\pi\sqrt{L_0 C}$, is the timescale on which the external circuit naturally operates. When the ratio of the circuit time scale to the residence time is small ($\ll 1$), the external circuit attempts to transfer its energy faster than the current sheet can accept it, leading to an inefficient acceleration process. On the other hand, when the ratio of the time scales is large ($\gg 1$), the sheet moves away from the acceleration coil quickly, exiting the acceleration region and decoupling before the external circuit can transfer the maximum amount of energy to the sheet. Between these two cases exists an optimum value of α where the current sheet's residence time scale is matched to the external circuit, allowing for optimum transfer of stored electrical energy into directed kinetic energy.

IV. Nondimensional Solutions

A. Solution Strategy

The set of coupled first-order ordinary differential equations (ODEs) given in (10) can be solved numerically once the mass

distribution and the set of scaling parameters given in (11) are specified. The performance metrics chosen for this study are the exhaust velocity, v_z^*, and the thrust efficiency, which is written in terms of nondimensional parameters as

$$\eta_t = \frac{m^* v_z^*}{2L^* \alpha}.$$

In solving any set of first-order (in time) differential equations, it is important to know when the time histories of the computed variables (specifically v_z^* in our case) should be queried to calculate performance. This question is, in fact, critical to the evaluation of these accelerators. For our nondimensional model, the integration period will end when one of the two following conditions is reached:

1) the end of the first half-cycle of the accelerator coil discharge is reached and the current I_1^* reverses in sign;
2) the sheet travels three characteristic lengths, $z^* = 3$.

The first condition above is based on the fact that when the accelerator current goes through zero, it is going though a point of high dI_1/dt. While the acceleration model does not incorporate any ionization physics, it is well known that a new current sheet can form at the face of the coil, causing what is known as a "crowbar discharge." If this occurs, the initial current sheet ceases to undergo acceleration.

The second condition stems from the existence of a finite axial distance between the current sheet and the coil, beyond which the two are essentially decoupled electrically. The separation distance $z^* = 3$ is chosen as our cutoff for electromagnetic coupling as it represents an inductance change in the circuit of 95% of the coil inductance. Above this cutoff value, the integration yields no significant change to the calculated performance.

If the propellant is not loaded like as a slug mass, more effort may be required to include propellant utilization inefficiencies in the total thrust efficiency. To do this, the velocity must be allowed to continue to evolving until all the available mass is entrained by the sheet. However, it should be clear from the above conditions that the calculation may halt before this occurs. If this is the case, the unentrained mass represents a mass utilization inefficiency in the acceleration scheme and the final values of v_z^* and m^* must be corrected to reflect this fact.

The correction begins by realizing that once the sheet is "decoupled," there is no mechanism by which it can transfer impulse to the thruster. However, we shall assume that the sheet continues to entrain the mass it encounters. When the computation is halted, the current sheet has entrained an amount of mass equal to m_f^* and is moving at a velocity equal to $(v_z^*)_f$, where the subscript f is used to indicate that these values are the final data points obtained from the numerical solution. The total mass available to the sheet is m_{bit}^*. Conservation of linear momentum is used to compute the corrected sheet velocity as

$$v_z^* = \frac{m_f^*}{m_{\text{bit}}^*} (v_z^*)_f . \tag{13}$$

B. Solutions

We present contour plots of computed performance (v_z^* and η_t) found by solving the nondimensional governing equations while varying the values of the various similarity parameters. The results are presented primarily for a slug mass loading ($\rho_A = 0$). The slug mass loading, while not physically realizable in a gas-fed system, allows for the exploration of the parameter space while minimizing the effects of the mass distribution on the acceleration scheme. The results from the slug mass loading are compared to a uniform fill ($\rho_A =$ constant for z^* between zero and three) and a triangular mass distribution equivalent to that found in the PIT [1] and given by

$$\rho_A = \begin{cases} \rho_0(1 - z/\delta_m), & z \le \delta_m \\ 0, & z > \delta_m \end{cases}$$

where $\delta_m/z_0 \approx 0.53$ in the PIT MkV. In all data sets, the baseline values of the nondimensional parameters are $L^* = 0.121$, $\psi_1 = 0.05$, $\psi_2 = 0.13$ and $\alpha = 2.1$. These values roughly correspond to those found in the PIT MkV accelerator [1].

Contour plots of computed efficiency and nondimensional exhaust velocity are presented for varying values of α and ψ_1 [Fig. 3(a), (b)], α and ψ_2 [Fig. 3(c), (d)], ψ_1 and ψ_2 [Fig. 4(a), (b)], and ψ_2 and L^* [Fig. 4(c), (d)]. We observe several important trends in these data.

First, in Fig. 3(a) and (c), we see that the efficiency possesses a local maximum with respect to α. Also, Fig. 3(b) and (d) show increasing sheet velocity with increasing α, implying a decrease in the residence timescale of the current sheet in the acceleration region. These observations are consistent with our interpretation of α as a dynamic impedance matching parameter.

Efficiency and exhaust velocity increase with decreasing ψ_1 and ψ_2 [Fig. 4(a), (b)]. This trend will be discussed in more detail in the next section. In addition, efficiency also increases with decreasing L^* showing the importance of increasing the ratio L_C/L_0 in a pulsed electromagnetic accelerator.

In Fig. 3(c) and (d) and Fig. 4(a) and (b), we observe a transition point in the solution near $\psi_2 = 3$. This transition is marked by a dashed line in the plots. Similarly, a transition in the solution form is marked by a dashed line in Fig. 4(c) and (d). In Section III, we discussed the physical meanings and interrelationships between ψ_1, ψ_2 and L^* by linearizing the circuit equations and finding solutions to a limiting case. We found that this linearization held when $\psi_2^2 L^* \ll 1$ and $\psi_2 L^* \ll 1$. For the present value of L^*, the more stringent requirement is the former. In Fig. 3(c) and (d) and Fig. 4(a) and (d), a dashed line given by the equation $\psi_2^2 L^* = 1$ is plotted. As the values of either ψ_2 or L^* increase, the nonlinear interactions between I_1 and I_2 increasingly affect the solution causing the time-history of I_2 to increasingly deviate from that of I_1. The same analysis showed that the quantity $\Psi = (\psi_1 + \psi_2)/2$ was important in determining the oscillatory nature of the current waveforms. We speculated that so long as the linearizing assumptions held, contours of constant performance should follow contours of Ψ equal to a constant. In general, we observe this to be true in the lower left-hand corners of Fig. 4(a) and (b).

We observe that propellant loading has a large influence on the thrust efficiency, going from a maximum of 70% for a slug mass [Fig. 3(a)] to 50% for a triangular mass loading [Fig. 5(a)] and 16% for a uniform fill [Fig. 5(b)]. These extreme cases help

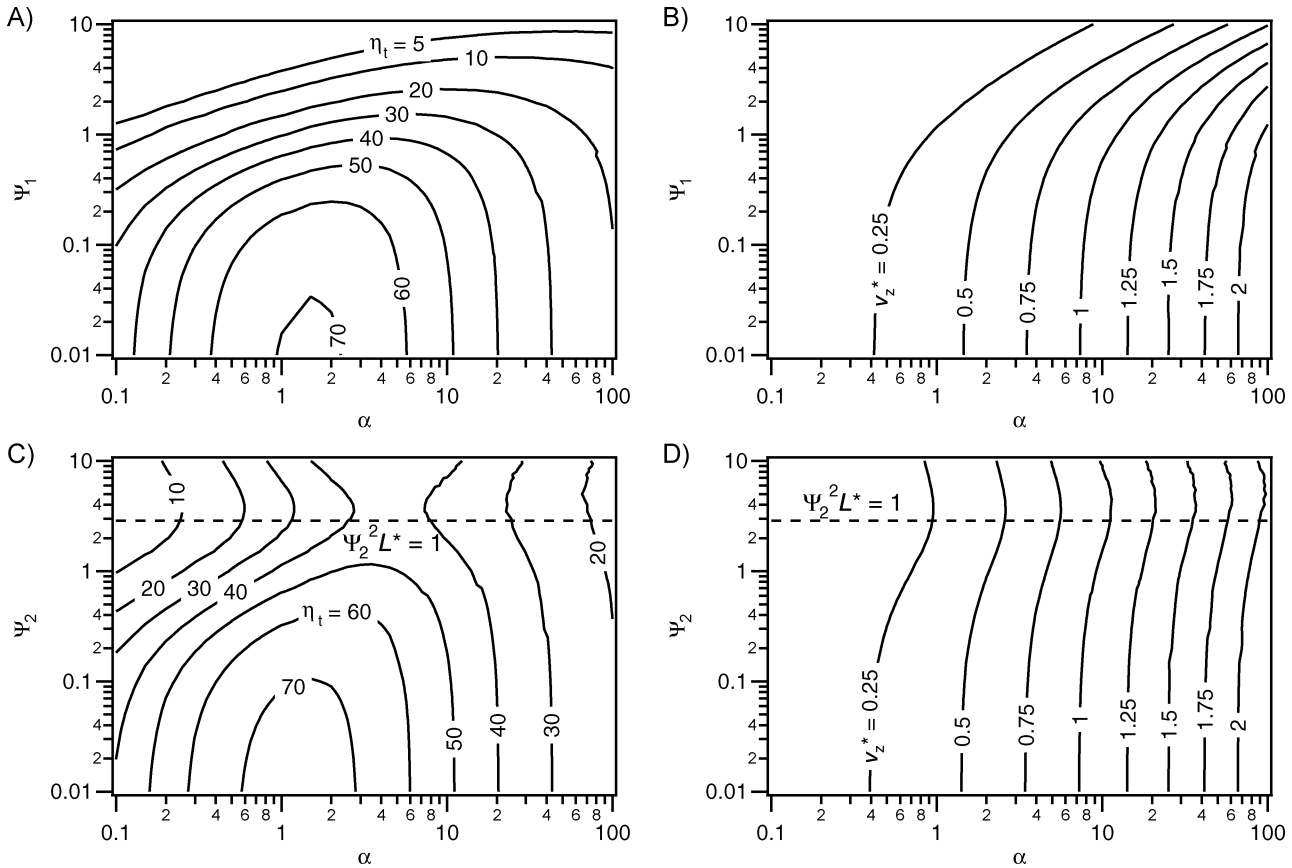

Fig. 3. Contour plots of inductive accelerator efficiency and nondimensional exhaust velocity for a slug mass loading found while varying: a) and b) α and ψ_1, c) and d) α and ψ_2. The other nondimensional values use to compute these data are: plots a) and b) $\psi_2 = 0.13, L^* = 0.121$; plots c) and d) $\psi_1 = 0.05, L^* = 0.121$.

emphasize the detrimental effects of drag on the current sheet as it entrains propellant. The performance is especially poor in the uniform fill case since much of the propellant is acquired after the circuit experiences a significant increase in inductance. Consequently, a current sheet with substantial velocity but little momentum propagates into the remaining propellant and experiences significant drag (drag force $\propto (v_z^*)^2$) while at the same time the driving force is decreasing exponentially with increasing axial position.

It is interesting to note that there is only a small amount of variation in the value of α that yields peak efficiency when comparing Fig. 3(a) and Fig. 5. The peak slowly shifts from α between 1 and 2 for a slug mass loading to between 2 and 3 for the uniform fill. The corresponding nondimensional parameters for PIT MkV data are plotted as "+" symbols in Fig. 5(a) and the measured thrust efficiencies associated with these points compare quite favorably with the computed performance contours in that graph. These data also show that the optimum α values are easily accessible experimentally.

V. Implications of the Results

Several observations made in the previous section lead directly to ways in which the performance of a pulsed inductive accelerator can be improved. First, an accelerator can achieve maximum efficiency when operated at or near values of α which allow for a good dynamic impedance match. It was shown in Fig. 3(a) and Fig. 5 that the optimum occurs when $1 \leq \alpha \leq 3$.

The value of L^* should be as low as possible to allow for as much electromagnetic acceleration as possible. In addition, the exhaust velocity can be increased by increasing the value of α.

The scaling with ψ_1 and ψ_2 is somewhat counterintuitive based on previous experience with pulsed plasma thrusters [12]. In PPTs the thrust efficiency decreases as a function of an increasing critical resistance ratio, which is similar to what we observe in Fig. 3(a) and (c) and Fig. 4(a). However, unlike the trends in PPT scaling where the thruster exhaust velocity decreases with decreasing ψ [12], the dimensionless exhaust velocity remains fairly constant as either ψ_1 or ψ_2 are varied independent of each other [Fig. 3(b) and (d)]. This is because the term that really matters as far as controlling the discharge waveform is Ψ (see Section III-B). In addition, the dimensionless exhaust velocity actually *increases* as *both* ψ_1 and ψ_2 (or Ψ) decrease in value [Fig. 4(b)]. Based on this scaling we must ask ourselves if we should attempt to operate a real pulsed inductive accelerator in the low ψ_1, ψ_2 regime.

Plotted in Fig. 6 are computed time histories of the various nondimensional parameters. To generate these curves, the equation set was integrated for different values of $\psi_1 = \psi_2$ while maintaining α and L^* constant. We observe two features in these data. The first is that the current waveforms do ring more as the values of ψ_1 and ψ_2 are decreased. This is evidenced in both the peak currents reached (both I_1^* and I_2^*) and the amount of voltage reversal after the first half-cycle and is an expected result based upon the analysis which yielded (13) and the dimensionless parameter Ψ. However, even though the

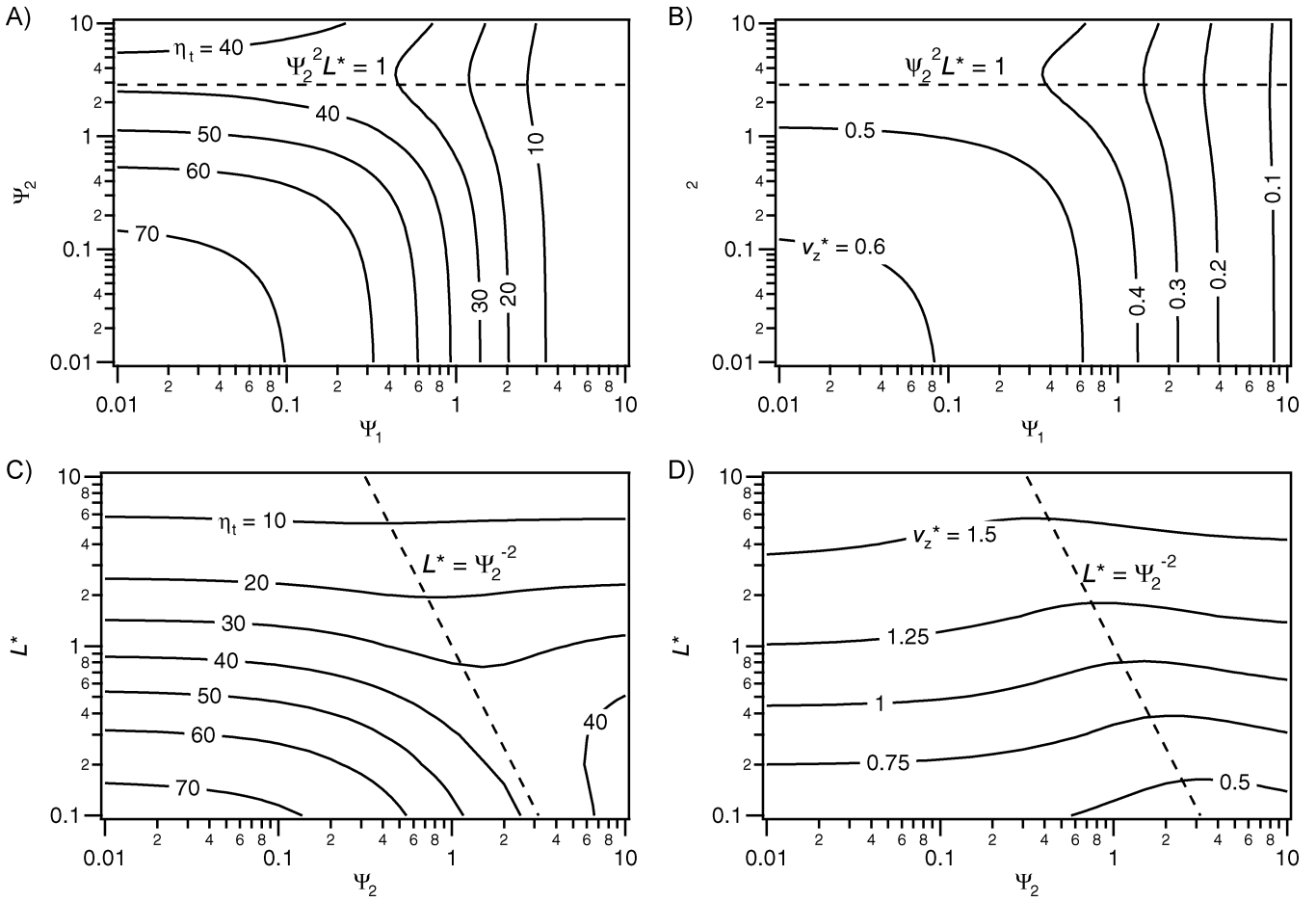

Fig. 4. Contour plots of inductive accelerator efficiency and nondimensional exhaust velocity for a slug mass loading found while varying: a) and b) ψ_1 and ψ_2, c) and d) ψ_2 and L^*. The other nondimensional values use to compute these data are: plots a) and b) $\alpha = 2.1$, $L^* = 0.121$; plots c) and d) $\alpha = 2.1$ and $\psi_1 = 0.05$.

circuit rings more (i.e., more energy returns to the capacitor at the end of the first half-cycle), the directed kinetic energy of the sheet and the thrust efficiency also increase as ψ_1 and ψ_2 decrease.

To explain this, we first note that α is invariant in these solution sets. Taking the interpretation of α as the dynamic impedance allows us to state, in rough terms, that the source (driving circuit) and the load (current sheet) are still approximately matched in all three cases plotted in Fig. 6. Consequently, we still obtain a high degree of energy transfer between the circuit and the load, even as ψ_1 and ψ_2 are decreased in value. This is why the solutions for the three cases, especially those for I_1 and I_2, while differing in magnitude, qualitatively behave in a similar fashion.

To explain the increase in exhaust velocity and thrust efficiency with decreasing ψ_1 and ψ_2, we recall that in pulsed plasma thrusters

$$\text{Impulse bit} \sim \int I^2 dt.$$

As the PPT circuit is adjusted from underdamped to critically damped, the peak current decreases. However, the total integral, and hence the impulse bit, and to some extent the thrust efficiency, can be conserved. On the other hand, in a pulsed inductive accelerator

$$\text{Impulse bit} \sim \int I_1^2 e^{-z(t)} dt.$$

This indicates that to improve impulse bits and thrust efficiencies, the current must peak while the sheet is still close to the back-end of the accelerator (i.e., near $z = 0$). The force accelerating the sheet drops exponentially as the sheet moves away from $z = 0$, *even if the peak current is maintained*. Therefore, to achieve efficient pulsed inductive acceleration, the highest possible peak current must be reached before the sheet moves far from $z = 0$. This implies that any attempts to lower the peak current and extend the current pulse length (either by increasing ψ_1 and ψ_2 to obtain a critically damped circuit or through the use of solid-state switching technology) will result in a less efficient acceleration process with a higher fraction of the total energy lost in the circuit through resistive dissipation.

There are several reasons why PPTs typically avoid the low critical resistance ratio, underdamped circuit regime. The missions for which PPTs are best suited require high specific impulse, so the exhaust velocity must be high. Also, the ringing circuit can result in a large voltage reversal which can be damaging to the lifetime of the capacitor. In addition, ringing circuits

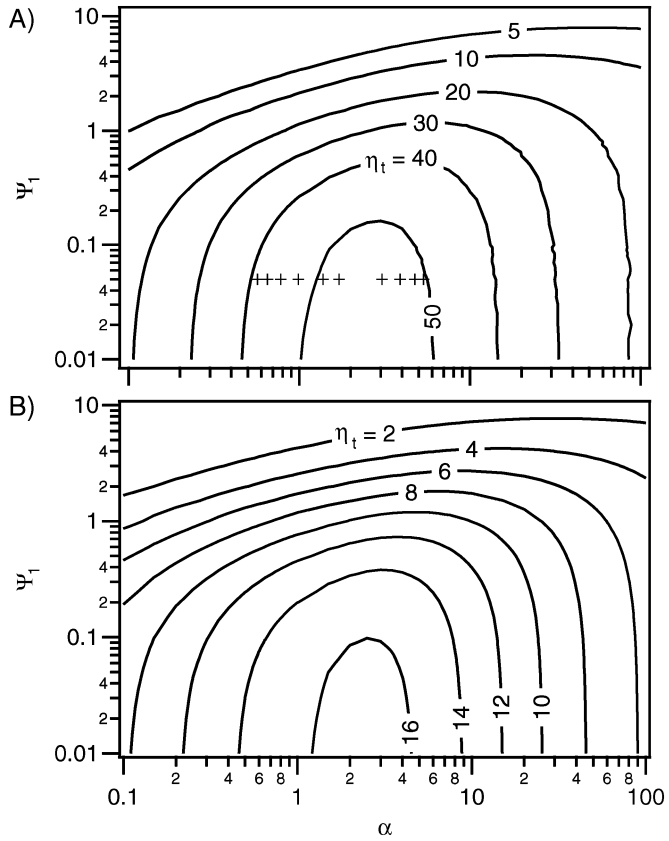

Fig. 5. Contour plots of inductive accelerator efficiency for (a) a triangular mass distribution and (b) a uniform mass distribution. Fixed nondimensional parameters in these computations are $\psi_2 = 0.13$, $L^* = 0.121$. Points corresponding to the nondimensional parameters found in the PIT MkV [1] are plotted in (a) and are indicated by "+" symbols. Measured thrust efficiencies associated with these points compare quite favorably with the computed performance contours.

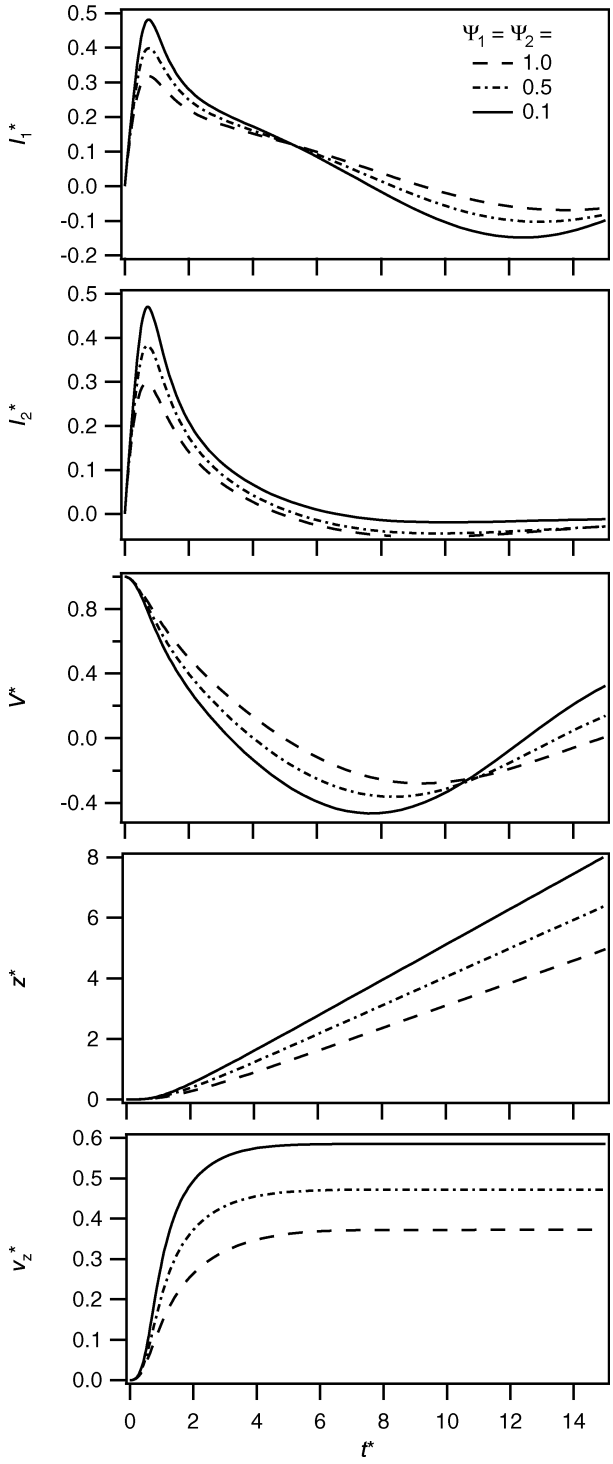

Fig. 6. Time histories of the various computed parameters in a pulsed inductive accelerator for different values of $\psi_1 = \psi_2$. Slug mass loading is employed and the values of α and L^* are 2.1 and 0.121, respectively.

can result in crowbar discharges which short-circuit the acceleration process before the current sheet reaches the ends of the electrodes.

In pulsed inductive accelerators, the problem of crowbar discharges can be avoided by maintaining a good dynamic impedance match. High specific impulses and efficiencies are realized in the low ψ_1, ψ_2 circuit configuration. The only remaining concern pertains to the capacitor voltage reversal. The voltage reversal for the data presented in Fig. 6 ranges from 20% of the maximum charge for $\psi_1 = \psi_2 = 1$ to 40% of the maximum charge for $\psi_1 = \psi_2 = 0.1$. It may be possible to reduce this by adjusting the values of L^* and α slightly. This implies that for high performance, a pulsed inductive accelerator should be operated in an underdamped mode. This may require the capacitor to handle a higher voltage reversal than in the critically damped mode.

VI. Conclusion

We have presented a nondimensional acceleration model for a pulsed inductive plasma accelerator. The nondimensionalization of the governing equations led to the identification of several performance scaling parameters, many of which have analogous counterparts from previous pulsed plasma thruster nondimensional acceleration models. The physical meanings of the scaling parameters and their effects on accelerator performance were explored through a series of theoretical arguments and numerical solutions. The analysis leads to the following insights.

- There exists a value of the dynamic impedance parameter, α for which thrust efficiency is maximized. This value is between 1 and 2 for a slug mass loading and 2 and 3 for the uniform fill. This optimum corresponds to a matching of the driving circuit's natural oscillation time scale to the

residence time scale of the current sheet in the acceleration zone.

- Efficiency increases for decreasing values of the inductance ratio, L^*, as this represents an increase in the fraction of energy which can be deposited into electromagnetic acceleration of the propellant.
- Efficiency and exhaust velocity increase when both ψ_1 and ψ_2 (or equivalently Ψ) are decreased in value. The reason is due to the scaling of the performance with $\int I_1^2 e^{-z(t)} dt$ which implies that the current must peak while the sheet is still close to the back end of the accelerator (i.e., near $z = 0$). Consequently, the greater initial currents found in underdamped circuits (relative to critically damped circuits operating at the same discharge energy) are preferable for higher performance.
- Performance increases as a greater fraction of the propellant is loaded close to the back-end of the accelerator and is maximized for a slug mass loading. This is primarily due to the drag associated with a moving current sheet entraining and accelerating any propellant it encounters.

ACKNOWLEDGMENT

The authors acknowledge K. Sankaran and T. Markusic for several helpful discussions and comments provided during the preparation of this work.

REFERENCES

[1] C. L. Dailey and R. H. Lovberg, The PIT MkV pulsed inductive thruster TRW Systems Group, Tech. Rep. NASA CR-191155, Jul. 1993.

[2] E. Y. Choueiri and K. A. Polzin, "Faraday acceleration with radiofrequency assisted discharge," *J. Propulsion Power*, accepted for publication.

[3] R. G. Jahn, *Physics of Electric Propulsion*. New York: McGraw-Hill, 1968.

[4] J. K. Ziemer and E. Y. Choueiri, "Scaling laws for electromagnetic pulsed plasma thrusters," *Plasma Sources Sci. Technol.*, vol. 10, no. 3, pp. 395–405, 2001.

[5] R. H. Lovberg and C. L. Dailey, "Large inductive thruster performance measurement," *AIAA J.*, vol. 20, no. 7, pp. 971–977, Jul. 1982.

[6] I. Hrbud, M. LaPointe, R. Vondra, C. L. Dailey, and R. Lovberg, "Status of pulsed inductive thruster research," in *Proc. Space Tech. Int. Forum (STAIF) 2002 Conf. AIP Proc. 608*, M. S. El-Genk, Ed., Feb. 3–7, 2002, pp. 627–632.

[7] P. Mikellides and D. Kirtley, "MACH2 simulations of the Pulsed Inductive Thruster (PIT)," presented at the 38th AIAA/ASME/SAE/ASEE Joint Propulsion Conf., Indianapolis, IN, Jul. 7–10, 2002, 2002-3807.

[8] P. Mikellides and C. Neilly, "Pulsed inductive thruster, Part 1. Modeling, validation and performance analysis," presented at the 40th AIAA/ASME/SAE/ASEE Joint Propulsion Conf., Ft. Lauderdale, FL, Jul. 11–14, 2004, 2004-4091.

[9] D. Allison and P. Mikellides *et al.*, "Pulsed inductive thruster, Part 2. A two-temperature thermochemical model for ammonia," presented at the 40th AIAA/ASME/SAE/ASEE Joint Propulsion Conf., Ft. Lauderdale, FL, Jul. 11–14, 2004, AIAA Paper 2004-4092.

[10] R. H. Lovberg and C. L. Dailey, "Current sheet development in a pulsed inductive accelerator," presented at the 25th AIAA/SAE/ASME/ASEE Joint Propulsion Conf., Monterey, CA, Jun. 10–12, 1989, Paper 89-2266.

[11] R. H. Lovberg, B. R. Hayworth, and T. Gooding, The use of a coaxial plasma gun for plasma propulsion Tech. Rep. AE62-0678, May 1962, G.D. Convair.

[12] J. K. Ziemer, "Performance scaling of gas-fed pulsed plasma thrusters," Ph.D. dissertation, Dept. Mechanical Aerospace Eng., Princeton Univ., Princeton, NJ, 2001.

Kurt A. Polzin received the Ph.D. degree from Princeton University, Princeton, NJ, in 2006, under the National Defense Science and Engineering Graduate Fellowship program.

He is a Research Scientist with the Propulsion Research Laboratory, NASA-Marshall Space Flight Center, Huntsville, AL. He is the author of several articles on pulsed plasma propulsion, liquid metal propellant feed systems, small-scale capillary flows, and geophysical fluid dynamics.

Edgar Y. Choueiri received the Ph.D. degree from Princeton University, Princeton, NJ.

He is Director of Princeton University's Electric Propulsion and Plasma Dynamics Laboratory and Director of PrincetonUniversity's Engineering Physics Program. He is Associate Professor in Applied Physics at the Mechanical and Aerospace Engineering Department, Princeton University, and Associated Faculty at the Department of Astrophysical Sciences (Program in Plasma Physics). He is the author of numerous articles on analytical, experimental, and numerical problems in electric and plasma propulsion, plasma physics and dynamics, instabilities and turbulence in collisional plasmas, plasma thruster numerical modeling, and applied mathematics.